

Nineteenth European Rotorcraft Forum

Paper No. C15

**NAVIER-STOKES SIMULATION OF ROTOR-BODY FLOWFIELD  
IN HOVER USING OVERSET GRIDS**

**G. R. Srinivasan and J. U. Ahmad**

JAI Associates, Inc.

465 Fairchild Drive, Suite 111

Mountain View, California 94043, U. S. A.

September 14-16, 1993

CERNOBBIO, (Como) ITALY

**ASSOCIAZIONE INDUSTRIE AEROSPAZIALI  
ASSOCIAZIONE ITALIANA DI AERONAUTICA ED ASTRONAUTICA**



# NAVIER-STOKES SIMULATION OF ROTOR-BODY FLOWFIELD IN HOVER USING OVERSET GRIDS

G. R. Srinivasan and J. U. Ahmad  
JAI Associates Inc.  
465 Fairchild Drive, Suite 111  
Mountain View, California 94043, U. S. A.

## ABSTRACT

A free-wake Navier-Stokes numerical scheme and multiple Chimera overset grids have been utilized for calculating the quasi-steady hovering flowfield of a Boeing-360 rotor mounted on an axisymmetric whirl-tower. The entire geometry of this rotor-body configuration is gridded-up with eleven different overset grids. The composite grid has 1.3 million grid points for the entire flow domain. The numerical results, obtained using coarse grids and a rigid rotor assumption, show a thrust value that is within 5% of the experimental value at a flow condition of  $M_{tip} = 0.63$ ,  $\theta_c = 8^\circ$ , and  $Re = 2.5 \times 10^6$ . The numerical method thus demonstrates the feasibility of using a multi-block scheme for calculating the flowfields of complex configurations consisting of rotating and non-rotating components.

## NOMENCLATURE

$a_\infty$	=	speed of sound, characteristic velocity scale
$b$	=	number of blades of the rotor
$c(r)$	=	blade chord at radial location $r$
$c_{eq}$	=	equivalent blade chord, $1/R \int_{R_1}^R c(r) dr$
$C_p$	=	pressure coefficient based on local dynamic pressure
$C_t$	=	sectional thrust coefficient based on local chord, $dt/dr/(c(r)q_{tip})$
$C_T$	=	rotor thrust coefficient, $T/(2\pi R^2 q_{tip})$
$dt$	=	incremental thrust
$dr$	=	incremental radial distance
$e$	=	energy per unit volume
$\hat{E}, \hat{F}, \hat{G}$	=	inviscid flux vectors
$IB$	=	I-blank array
$M_{tip}$	=	blade tip Mach number
$q_{tip}$	=	rotational dynamic pressure, $1/2 \rho (\Omega R)^2$
$\hat{Q}$	=	vector of conserved flow quantities
$r$	=	rotor radial coordinate
$R$	=	blade radius
$R_1$	=	blade radius at the root section
$Re$	=	Reynolds number based on $M_{tip}$ and $c_{eq}$
$\hat{S}$	=	viscous flux vector
$T$	=	rotor thrust
$u, v, w$	=	velocity components in physical space
$x, y, z, t$	=	physical space coordinates
$\theta_c$	=	collective pitch
$\rho$	=	density
$\sigma$	=	rotor geometric solidity, $b \int_{R_1}^R c(r) dr / (\pi R^2)$
$\xi, \eta, \zeta, \tau$	=	body-conforming coordinates of computational space
$\Omega$	=	rotor angular velocity

## 1. INTRODUCTION

The accurate prediction of aerodynamic loads and performance characteristics of a hovering rotor continues to be one of the most complex and challenging problems in applied aerodynamics. This is true even in the

absence of a fuselage or a rotor mounting body. The complexity of the flow stems from several peculiar features that are unique to a helicopter rotor; the dominant of these is the vortical wake, which strongly influences the operating characteristics. Accurate prediction of this vortical wake is probably the most important, the most studied, and the most difficult aspect of a helicopter flowfield. This gets further complicated in the presence of a fuselage or a rotor mounting device an account of its close proximity to the rotor. The fuselage presence alters the rotor wake trajectory due to its displacement effect, perhaps even influences the vortex structure. It thus alters the induced inflow and, hence, the performance.

Current methods of predicting hovering helicopter flowfields range in complexity from relatively simple boundary integral methods (Refs. 1-2) to more sophisticated computational fluid dynamics (CFD) methods (Refs. 3-12). Although there is hope that the CFD methods are the ones which eventually will replace all the simple semi-empirical methods for performance evaluation and design criteria, they are far from reaching that goal because of two important constraints. These are: a) accurate modeling of tip vortices and convecting them without significant numerical diffusion in finite-difference grids; b) requirements of large computer resources of memory and central processor Unit (CPU) time for any reasonably accurate answers. Also, these methods are still in the development stage, particularly for calculating the rotor-body interactional flowfields.

Many semi-empirical methods are currently being used in the helicopter industry for predicting airloads. These methods have limited application in that the empirical determination of wake shape ignores some of the important flowfield details such as the mutual interaction of individual vortical elements. The fact that these methods have to be coupled with some wake model for realistic estimates of airloads, they are, therefore, restricted in their application to blade shapes and planforms that are geometrically simple. Besides, some of these methods can not easily treat compressibility and transonic effects which is a feature of modern advanced helicopters with exotic blades.

The recent trend in the application of CFD methods to predict these complex flows has opened a new avenue to predict and understand the flow physics better. Methods based on the solutions of full-potential, the Euler, and the Navier-Stokes equations abound in the literature. Although most of these methods still use some wake model to bring in the influence of vortical wake, there are methods that capture the effects of wake fairly accurately as a part of the overall flowfield. In this regard, the recent methods based on the solutions of full-potential (Refs. 3-4), the Euler (Refs. 5-8) and the Navier-Stokes (Refs. 8-10) equations are noteworthy.

The above discussion is true for isolated helicopter rotors (without fuselage). The presence of a fuselage or a rotor-mounting device complicates the problem further. All previous treatments of the rotor-body problem have been either boundary integral methods (Refs. 13-14) or CFD methods which treat the rotor as an actuator disc (Refs. 15-16) and hence does not have to deal with the problem of convecting vortical flow in the presence of numerical diffusion associated with the CFD methods. Although Ref. 16 uses a Navier-Stokes method, it calculates the global time-averaged wake alone by prescribing the details of the flow on the rotor itself. In contrast, in the potential flow method used in Ref. 17 to study the same rotor-body problem, considered here, the flow solver is coupled with a "free" wake, in which the wake vorticity is specified, but is allowed to convect freely with the flow without constraining its trajectory. The other recent CFD methods (Refs. 5-10) developed for helicopter rotors use direct techniques for the entire flowfield without having to model wake separately. But these methods have not been extended to calculate rotor-body flows yet.

In the present study, the Navier-Stokes method of TURNS (Transonic Unsteady Rotor Navier-Stokes) developed for helicopter rotors (Refs. 8 and 18) will be used to develop a multi-block Navier-Stokes flow solver for calculating the rotor-body flows using structured overset Chimera grids to describe the complete flowfield. The preliminary work of extending TURNS code to using multiple (three) embedded grids was completed in Ref. 10, where it was used to calculate the hovering flowfield of a two-bladed rotor. The rotor-body problem being considered here is the same as the one studied by Ramachandran et al. (Ref. 17) using a potential flow method of Helix. The fundamental difference between the two approaches lies in the way the actual whirl-tower is included in the calculations. The present method considers the actual whirl-tower as a solid body. In contrast, the study of Ref. 17 treats the whirl-tower as a structured circulation sheet and the strength of the sheet was determined by an iterative procedure. The actual whirl-tower was thus not included in the flow topology.

The use of the Navier-Stokes method enhances (a) the tip flow simulation which involves resolving the three-dimensional separated flow and concentrated tip vortex, and (b) the accurate simulation of strong viscous-inviscid interaction involving shock-induced separation at high tip speeds. Currently the vortical structure calculated with this method using a single-block grid is smeared due to grid coarseness (Ref. 8). However, the nearfield wake trajectory and circulation are captured fairly accurately.

## 2. GOVERNING EQUATIONS AND SOLUTION METHOD

The governing partial differential equations are the unsteady, thin-layer Navier-Stokes equations. For generality, these equations are written in strong conservation-law form in generalized body-conforming curvilinear space  $(\xi, \eta, \zeta, \tau)$  (Refs. 8 and 19) and are given by

$$\partial_\tau \widehat{Q} + \partial_\xi \widehat{E} + \partial_\eta \widehat{F} + \partial_\zeta \widehat{G} = Re^{-1} \partial_\zeta \widehat{S} + \mathfrak{R} \quad (1)$$

where

$$Q = [\rho, \rho u, \rho v, \rho w, e]^T, \text{ and}$$

$$\widehat{Q} = Q/J$$

Here  $Q$  is the flowfield vector of conserved quantities,  $\widehat{E}$ ,  $\widehat{F}$ ,  $\widehat{G}$  are the inviscid convective flux vectors,  $\widehat{S}$  is the viscous flux vector considered in the thin layer limit, and  $\mathfrak{R}$  is a source term that is added to account for the centrifugal force of rotation of the blade. Also,  $J$  is the Jacobian of transformation,  $Re$  is the Reynolds number and the sign  $\widehat{\phantom{x}}$  indicates that the quantity is normalized by the Jacobian. The primitive variables of Eq. (1) are the density  $\rho$ , the three mass fluxes  $\rho u$ ,  $\rho v$  and  $\rho w$  in the three coordinate directions  $x$ ,  $y$  and  $z$ , respectively and the energy per unit volume  $e$ . All these quantities are nondimensionlized by the appropriate free stream reference quantities. The root chord  $c$  of the rotor blade and the free stream sound speed  $a_\infty$  are assumed to be the characteristic length and velocity scales. The equation set given by Eq. (1) together with the equation of state for a perfect gas

$$p = (\gamma - 1) \left\{ e - \frac{\rho}{2} (u^2 + v^2 + w^2) \right\} \quad (2)$$

describe the entire flowfield.

The finite-difference implicit numerical scheme used for the solution of Eq. (1) is called TURNS and is described in Ref. 8. Its application to calculate aerodynamics and acoustics (high speed impulsive noise) of helicopter rotors in hover and forward flight is described in Ref. 18. In the numerical algorithm, the evaluation of inviscid fluxes is based on an upwind-biased flux-difference split scheme with a monotone upstream-centered approach used to obtain a third-order accurate scheme with flux limiters that model shocks and propagate acoustics accurately. The use of Roe's upwinding eliminates the addition of explicit numerical dissipation and thus produces a less dissipative numerical scheme. The use of a lower-upper symmetric Gauss-Seidel (LU-SGS) implicit operator makes the numerical scheme computationally efficient as well as robust. The option of Newton sub-iterations at each time-step reduces the linearization and factorization errors as well as makes the numerical scheme second-order accurate in time, and this is particularly useful for unsteady (forward flight) calculations. Currently the scheme is third-order accurate in space and first- or second-order accurate in time.

To take advantage of the quasi-steady nature of the hovering rotor flowfield, the governing equations are solved in the blade-fixed coordinate system. This necessitates adding source terms to account for the centrifugal force of rotation of the blades. In addition to the source term  $\mathfrak{R}$  added to the right side of the numerical algorithm, a source term Jacobian is added to either the Lower or Upper operator of the implicit LU operator (see Ref. 8). Further, a locally-varying time-step is used in the integration procedure to accelerate convergence (Ref. 20) of the numerical scheme.

Modifications to the single-block grid algorithm of TURNS are needed to accommodate multiple Chimera overset grids. A general outline of this implementation is described by Steger et al. (Ref. 21). The implementation of this procedure in the TURNS algorithm was first done by Duque and Srinivasan (Ref. 10). Using this modified algorithm, the study used a three-grid option (two embedded grids in a global grid) to calculate the hovering flow of an isolated rotor blade. This logic has been further modified in the present study to model a rotor mounted on a central whirl-tower. With these modifications, a large number of overset Chimera grids can be used to model any complex flowfield containing rotating and non-rotating components. Also, the parameter statements in the code have been reordered to optimize the code for efficiency.

Briefly, the method is as follows. A large number of subordinate grids are generated for resolving various individual elements of the of the surface geometry and the flowfield such as boundary layers, vortical flows, tip vortices, shocks, etc. These grids are embedded within a global grid comprising of the entire flow domain. consequently, some of the grid points of the global grid fall within the solid body regions defined by the subordinate grids. When these points are removed, they create "holes" within the larger grid. The data at these hole boundaries are linearly interpolated for subordinate grid and global background grid by using each others data.

As explained above, to allow for the presence of holes within the interior of a grid requires modifications to the basic TURNS algorithm. The locations of the hole points are made available by introducing an I-blank array, IB. This variable IB takes on an interger value of 0 when the grid point in question is a hole point or 1 otherwise. The I-blank array is introduced on both left and right sides of the numerical algorithm such that the solutions at hole points equal 0 (see Ref. 10). The following will illustrate how this is done for the right hand side of the numerical algorithm.

The application of Roe's upwinding to the numerical flux of the inviscid terms results in the locally one-dimensional form and can be written, e.g., in the  $\xi$  direction, as

$$\begin{aligned} \widehat{E}(Q_L, Q_R, (\nabla\xi/J)_{j+\frac{1}{2}}) = \\ \frac{1}{2}[\widehat{E}(Q_R, (\nabla\xi/J)_{j+\frac{1}{2}}) + \widehat{E}(Q_L, (\nabla\xi/J)_{j+\frac{1}{2}})] \\ - |A(Q_L, Q_R, (\nabla\xi/J)_{j+\frac{1}{2}})|(Q_R - Q_L) \end{aligned} \quad (3)$$

where  $A$  is the Roe-averaged Jacobian matrix and  $Q_L$  and  $Q_R$  are the left and right state variables of the cell interface. The differencing scheme degenerates to the first-order accuracy at the grid boundaries. To accomodate this requirement with Chimera blanking, higher-order scheme are constructed from a one-parameter family of interpolations and I-blanks for the primitive variables  $\rho$ ,  $u$ ,  $v$ ,  $w$ , and  $p$ . For example, the left and right state variables for  $p$  are,

$$p_L = \left\{ 1 + \frac{\psi_j IB_j IB_{j-1}}{4} [(1 - \kappa)\nabla + (1 + \kappa)\Delta] \right\} p_j \quad (4a)$$

$$p_R = \left\{ 1 - \frac{\psi_{j+1} IB_{j+1} IB_{j+2}}{4} [(1 + \kappa)\nabla + (1 - \kappa)\Delta] \right\} p_{j+1} \quad (4b)$$

where  $\nabla$  and  $\Delta$  are backward and forward difference operators, and  $\kappa$  is a parameter that controls the construction of higher-order differencing schemes. For example,  $\kappa = \frac{1}{3}$  is used in the present method to construct the third-order scheme. The limiter  $\psi$  is calculated by using Koren's differentiable limiter (see Ref. 8) as

$$\psi_j = \frac{3\nabla p_j \Delta p_j + \epsilon}{2(\Delta p_j - \nabla p_j)^2 + 3\nabla p_j \Delta p_j + \epsilon} \quad (5)$$

where a small constant, typically  $\epsilon = 10^{-6}$ , is added to prevent the division by zero. Similar formulae are used for the other primitive variables. The viscous flux terms are discretized using standard second-order central-differencing (Ref. 19). Finally, the calculations reported here assume fully turbulent flow for the blades and the whirl-tower and laminar flow in the wake. The simple algebraic turbulence model of Baldwin and Lomax (Ref. 22) is used to estimate the eddy viscosity.

The coordinate transformation space metrics are evaluated using a finite volume formulation. This approach is known to preserve free-stream accurately in steady flows where time metrics are zero. However, use of this method to form time metrics rigorously has been found to be computationally expensive. Therefore, a finite-difference formulation is adopted for unsteady metrics. As a result, a free-stream subtraction of time metrics is then required to restore accuracy. With these features, the code is robust, fairly efficient, and runs at 145 MFLOPS on a Cray Y-MP supercomputer for a single-block grid and at 125 MFLOPS for the current eleven-block Chimera overset grids.

### 3. CHIMERA OVERSET GRIDS

The geometry of a 4-bladed Boeing 360 rotor mounted on a whirl-tower is considered as the rotor-body configuration for the present study. The surface geometry of this is shown in Fig. 1. The rotor diameter is 50 ft., the whirl-tower height is 44.5 ft., and the base of the tower has a diameter of 43 ft. The distance of the rotor above the ground is 50 ft. The blades of the rotor are long and slender with a 3:1 tip taper and an aspect ratio of 11.47. The blades are highly twisted and the radial twist distribution for this blade is shown in Fig. 2. The twists shown in Fig. 2 include a collective pitch of  $\theta_c = 8^\circ$ .

Body conforming finite-difference grids are used for the long slender blades of the Boeing 360 blade and the whirl-tower. C-H type grids were constructed for each of the blades by stacking 2-dimensional grids along its radius. A typical C-grid generated by a hyperbolic grid generation code (Ref. 23) is shown at the root section of one of the blades along with surface geometry in Fig. 3. The grid is clustered at the leading and trailing edges as well as at the surface of the blade to resolve boundary layer. A cosine distribution is used to

stack these C-grids in the spanwise direction. The grids extend about 2 chords in front and back of the blades and about 4 chords beyond the tip in the spanwise direction. Each blade grid has 101 points in the chordwise (wraparound) direction, 41 points in the radial direction, and 37 points in the normal direction. The spacing of the first grid point in the normal direction is 0.00005 of chord.

Body conforming grids are also generated for the tower and hub independently. Transition grids are constructed, one for each blade, to enable the blade flow to smoothly transit into the global grid and to improve interpolation between neighboring grids. Figure 4 shows a view of this global grid. The boundaries of transition grid around the blades are shown in blue, the blade grid surface is in light blue, the blade grid (shown at the tip and root sections) is in dark blue, the blade hub surface is in black, tower surface grid is in magenta, tower grid in section is in green, and farfield boundary grid is in red color. The farfield grid is located at two rotor diameters in the radial direction and two diameter above the ground surface. Figure 5 shows a view of the composite grid. The rotor hub grid is shown as a transition grid in green color. The extent of the blade transition grid is shown in blue color. The view clearly shows how the grids overlap on each other cutting in to neighboring grids and surfaces. Each of the single grids, including the global grid, has approximately the same total grid points. The composite grid has a total of about 1.3 million grid points comprising of 11 different blocks.

In overset grids, each individual grid within the global system is not overly constrained by the presence of multitude of boundaries and hence more uniform and well stretched grids can be generated. However, determining the hole points and the corresponding hole boundaries between the individual grids can become a difficult problem. The quality of the solution interpolation at the cell boundaries depends on the relative grid cell aspect ratio, grid skewness, and grid clustering. It also depends on the boundary's proximity to the high flow gradient regions. Therefore, while generating grids one must assure that there is enough overlap of the neighboring grids, and grid cells are approximately of equal aspect ratio with minimum skewness. If possible, the grid boundaries should be located away from the regions of high flow gradients. However, to achieve this often requires some ingenuity and creativity during the grid generation exercise.

To determine the connectivity between neighboring grids and the hole points in the present 11 grid system, an inverse mapping inter-grid communication procedure, also known as Domain Connectivity Function (DCF) (Ref. 24), is used. This procedure provides all the hole locations and interpolation coefficients to link the various overset grids. The DCF procedure is used instead of the static and dynamic PEGSUS codes (Ref. 25-26). The DCF procedure uses an inverse mapping of compartmental space to limit the search time to locate and compute hole interpolation stencils. Various analytic shapes are used to create holes. The creation of analytic shapes in DCF require negligible time and is therefore more efficient than PEGSUS. The major expense in DCF is in the creation of inverse maps. Even for the moving bodies this is one-time expense. Once the inverse maps are created, they are used repeatedly for the later stages of the grid movement and are independent of the relative orientation of the grids in the overset grid system. The search time required by DCF is an order of magnitude smaller than that is required by the PEGSUS procedure. Examples of hole boundaries generated by the DCF scheme for the Boeing-360 rotor, the hub, and the support tower are shown elsewhere (Ref. 27). Figure 6 shows the hole boundaries in the composite grid system consisting of 11 different grids for the rotor mounted on a whirl-tower.

#### 4. BOUNDARY CONDITIONS

All the boundary conditions are applied explicitly. At the blade surfaces, the blade hub surface, whirl-tower surface a no-slip boundary condition is used for the viscous calculations. The density at the wall is determined by a zeroth-order extrapolation. The pressure along the body surface is calculated from the normal momentum relation (see, for example, Ref. 19). The total energy is then determined from the equation of state. To ensure continuity across the wake cut and also outboard of the blade tip, where the grid collapses to a singular plane because of H-grid topology, the flow quantities are determined by averaging the flow variables from both sides of the singular plane. Characteristic-type boundary conditions are used at the farfield boundary.

Although the rotor operates in a quiescent fluid atmosphere, unlike in a fixed wing airplane, it induces significant velocities at large distances from the rotor. Therefore, specification of no flow at the inflow boundaries of a computational box, which is typically small for economy, poses a difficulty for the prediction methods. Prescription of no-flow condition at the farfield boundaries produces a "closed box" environment for the rotor where the flow recirculates within the computational "box". To overcome this situation, a simpler and more economical alternative was introduced in Ref. 9 using the concepts of a three-dimensional point-sink and simple momentum theory concepts as a guide. With this approach, the application of the above characteristic-type boundary condition produced a non-zero inflow at the farfield boundaries.

## 5. RESULTS AND DISCUSSION

As mentioned before, the geometry considered for the present Navier-Stokes calculations is the Boeing 360 rotor in a whirl-tower. This is exactly the same geometry considered by Ramachandran et al. (Ref. 17). The flow condition chosen for the present calculation is  $M_{tip} = 0.63$ ,  $\theta_c = 8^\circ$  and a Reynolds number based on the root chord and blade tip speed of  $Re = 2.5 \times 10^6$ . Unlike in the previous studies (Refs. 8-10), the hovering flowfield on the entire geometry is calculated without invoking any periodicity condition in the azimuthal direction. In the calculations, the rotor is set in motion from a quiescent flow condition with the whirl-tower stationary like in an experiment and the evolution of the flowfield to a quasi-steady state is monitored. Calculations were run for three-orders drop in the blade grid residuals which required about 1500 iterations. These calculations were performed on the CRAY-YMP (Eagle) supercomputer at NASA Ames Research Center and took about 14 of CPU hours to convergence on a 1.3 million points grid.

Figure 7 shows the surface pressure distributions at several radial stations along the blade. For this flow condition there were no shocks on the blade surface. The leading edge and trailing edge regions needed better grid resolution. As seen in the  $C_p$  plots, the leading edge peaks and the trailing edge region are not well resolved. There is flow separation on the inboard part of the blade and no separation in the outboard part except in the very tip region, which is of small extent. Figure 8 shows the sectional thrust distribution along the blade. It has the standard form, peaking towards the tip. Unfortunately, the experimental data was not available to compare this thrust distribution. However, the integrated rotor thrust is compared with the experimentally determined value as well as the calculations of Ref. 17. The present calculations gave a thrust value of  $C_T/\sigma = 0.084$ . This is about 5% more than the experimental value of 0.08. The potential flow free-wake calculations of Ramachandran et al. (Ref. 17) predicted a value of 0.07 for a similar rotor-body configuration. The rotor blades in this had different airfoil coordinates. However, the recent calculations performed by Ramachandran (Ref. 28) on an isolated rotor (without center body), using the same solution method as Ref. 17 and exactly the same blades used in the present study, gave a thrust value of 0.085. Thus, the comparison of the present Navier-Stokes results with both experiments and the calculations from HELIX (Ref. 28) indicate that the present approach of using multiple grids is a promising method for calculating the complex rotor-body flows.

Figure 9 shows a plot of the velocity vectors colored by the vertical velocity for the entire flowfield. As seen, there is a clear indication that the flow is coming from the farfield boundary and this flow along with the flow being pushed-up by the ground plane are being pushed down by the rotor. The coarse grids used in this investigation were unable to resolve the vortex sheet at the bottom of the tower. The tip vortex trajectory was very diffused beyond the transition grids. Overall, the velocity plot of Fig. 9 clearly indicates the fountain-type flow mechanism that is expected of this kind of geometry.

## 6. CONCLUDING REMARKS

A free-wake Navier-Stokes CFD methodology is developed for calculating the hovering flow of a rotor-body combination utilizing multiple Chimera overset grids. For the Boeing 360 rotor and whirl-tower configuration considered in this study, a total of eleven grids are used to represent the complete flowfield domain. The calculated thrust coefficient,  $C_T/\sigma = 0.084$ , is within 5% of the experimental value of 0.08 for this rotor configuration, which is assumed to have rigid blades, at the flow condition of  $M_{tip} = 0.63$ ,  $\theta_c = 8^\circ$ , and  $Re = 2.5 \times 10^6$ . The fair agreement of the calculated thrust with experiments indicates that this free-wake Navier-Stokes CFD capability, utilizing multiple overset grids, is a promising tool for analyzing complex configurations.

## 7. ACKNOWLEDGEMENTS

This work is supported by the NASA Ames Research Center under contract NAS2-13534. The authors would like to thank Earl P. N. Duque of the U. S. Army AFDD for some useful discussions and Drs. K. Ramachandran (Flow Analysis, Inc.) and Frank Caradonna (U. S. Army AFDD) for providing the geometry of the Boeing 360 rotor and whirl tower.

## 8. REFERENCES

1. A. J. Landgrebe, An Analytical and Experimental Investigation of Helicopter Rotor Hover Performance and Wake Geometry Characteristics, USAAMRDL TR-71-24, U. S. Army, June 1971.
2. F. F. Felker, T. R. Quackenbush, D. R. Bliss, and J. S. Light, Comparisons of Predicted and Measured Rotor Performance in Hover Using a New Free Wake Analysis, *Proceedings of the 44th Annual Forum of the American Helicopter Society*, Washington, D. C., June 1988.

3. K. Ramachandran, C. Tung, and F. X. Caradonna, Rotor Hover Performance Prediction Using a Free-Wake Computational Fluid Dynamics Method, *Journal of Aircraft*, Vol. 26, No. 12, Dec. 1989, pp. 1105-1110.
4. C. Tung and K. Ramachandran, Hover Performance Analysis of Advanced Rotor Blades, *Proceedings of the 48th Annual Forum of the American Helicopter Society*, Washington, D. C., June 1992, pp. 1367-1384.
5. E. Kramer, J. Hertel, and S. Wagner, Euler Procedure for Calculation of the Steady Rotor Flow with Emphasis on Wake Evolution, AIAA Paper 90-3007, AIAA 8th Applied Aerodynamics Conference, August 1990, Portland, Oregon.
6. C. L. Chen and W. J. McCroskey, Numerical Simulation of Helicopter Multi-Bladed Rotor Flow, AIAA Paper 88-0046, AIAA 26th Aerospace Sciences Meeting, January 1988, Reno, Nevada.
7. R. C. Strawn and T. J. Barth, A Finite-Volume Euler Solver For Computing Rotary-Wing Aerodynamics on Unstructured Meshes, *Proceedings of the 48th Annual Forum of the American Helicopter Society*, Washington, D. C., June 1992, pp. 419-428.
8. G. R. Srinivasan, J. D. Baeder, S. Obayashi, and W. J. McCroskey, Flowfield of a Lifting Rotor in Hover - A Navier-Stokes Simulation, *AIAA Journal*, Vol. 30, No. 10, October 1992, pp. 2371-2378.
9. G. R. Srinivasan, V. Raghavan, and E. P. N. Duque, Flowfield Analysis of Modern Helicopter Rotors in Hover by Navier-Stokes Method, *Proceedings of the International Technical Specialists Meeting on Rotorcraft Acoustics and Rotor Fluid Dynamics*, October 1991, Philadelphia, Pennsylvania.
10. E. P. N. Duque and G. R. Srinivasan, Numerical Simulation of a Hovering Rotor Using Embedded Grids, *Proceedings of the 48th Annual Forum of the American Helicopter Society*, Washington, D. C., June 1992, pp. 429-445.
11. B. E. Wake and L. N. Sankar, Solutions of the Navier-Stokes Equation for the Flow About a Rotor Blade, *Journal of the American Helicopter Society*, Vol. 34, No. 2, April 1989, pp. 13-23.
12. R. K. Agarwal and J. E. Deese, Navier-Stokes Calculations of the Flowfield of a Helicopter Rotor in Hover, AIAA Paper 88-0106, 1988.
13. D. R. Clark and B. Maskew, Study for Prediction of Rotor/Wake/Fuselage Interference - Part I", NASA CR 177340, March 1985.
14. T. A. Egolf and P. F. Lorber, Unsteady Rotor/Fuselage Interaction Method, *Proceedings of the American Helicopter Society National Specialists Meeting on Aerodynamics and Aeroacoustics*, Arlington, Texas, February 1987.
15. T. Q. Dang, Calculations of Propeller/Airframe Interference Effects Using the Potential/Multienergy Flow Method, *AIAA Journal*, Vol. 28, No. 5, May 1990, pp. 771-777.
16. L. A. J. Zori, S. R. Mathur, and G. Rajagopalan, Three-Dimensional Calculations of Rotor-Airframe Interaction in Forward Flight, *Proceedings of the 48th Annual Forum of the American Helicopter Society*, Washington, D. C., June 1992, pp. 489-512.
17. K. Ramachandran, F. X. Caradonna, and J. Steinhoff, The Free-Wake Computation of Rotor-Body Flows, AIAA Paper 90-1540, AIAA 21st Fluid Dynamics, Plasma Dynamics and Lasers Conference, June 1990, Seattle, Washington.
18. G. R. Srinivasan and J. D. Baeder, Recent Advances in Euler and Navier-Stokes Methods for Calculating Helicopter Rotor Aerodynamics and Acoustics, *Proceedings of the Fourth International Symposium on Computational Fluid Dynamics*, September 1991, Davis, California, pp. 1095-1100.
19. T. H. Pulliam and J. L. Steger, Implicit Finite-Difference Simulations of Three-Dimensional Compressible Flow, *AIAA Journal*, Vol. 18, No. 2, February 1980, pp. 159-167.
20. G. R. Srinivasan, W. J. Chyu, and J. L. Steger, Computation of Simple Three-Dimensional Wing-Vortex Interaction in Transonic Flow, AIAA Paper 81-1206, AIAA 14th Fluid and Plasma Dynamics Conference, June 1981, Palo Alto, California.
21. J. L. Steger, F. C. Dougherty, and J. A. Benek, A Chimera Grid Scheme, *Advances in Grid Generation*,

22. B. S. Baldwin and H. Lomax, Thin Layer Approximation and Algebraic Model for Separated Turbulent Flow, AIAA Paper 78-0257, AIAA 16th Aerospace Sciences Meeting, January 1978, Huntsville, Alabama.

23. T. J. Barth, T. H. Pulliam, and P. G. Buning, Navier-Stokes Computations for Exotic Airfoils, AIAA Paper 85-0109, Reno, Nevada, January 1985.

24. R. Meakin, A New Method For Establishing Inter-Grid Communication Among Systems of Overset Grids, AIAA Paper 91-1586, Honolulu, Hawaii, June 1991.

25. R. Meakin and N. Suh, Unsteady Aerodynamic Simulation of Multiple Bodies in Relative Motion, AIAA Paper 89-1996, Buffalo, New York, June 1989.

26. J. Benek, T. Donegan, and N. Suh, Extended Chimera Grid Embedding Scheme with Application to Viscous Flows, AIAA Paper 87-1126-CP, 1987.

27. G. R. Srinivasan and J. U. Ahmad, Navier-Stokes Simulation of Rotor-Body Flowfield, Part 1: Hover, JAI Associates, Inc. Tech. Report, JAIA TR-92-02, August 1992.

28. K. Ramachandran, Private Communication, Flow Analysis, Inc., NASA Ames Research Center, Moffett Field, California.

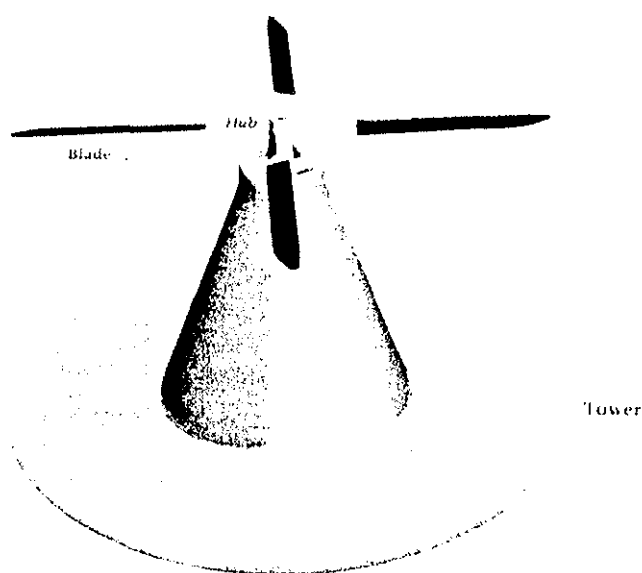


Fig. 1 Surface representation of the Boeing-360 rotor and whirl-tower.

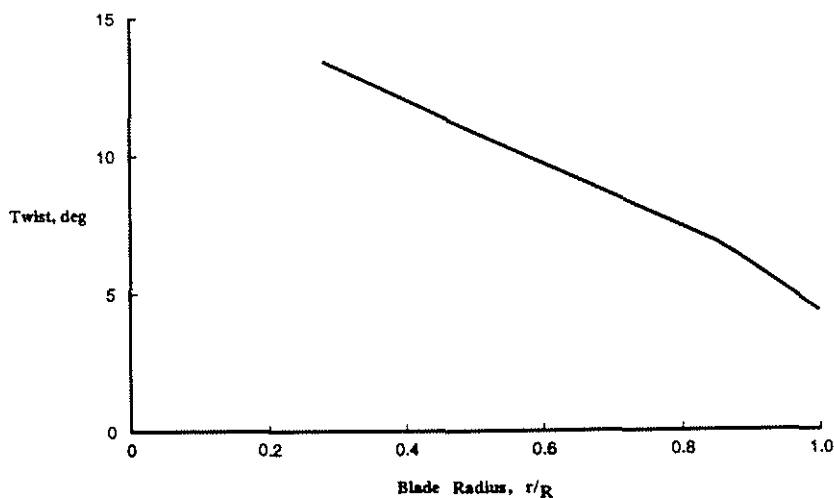


Fig. 2 Effective radial twist distribution of the rotor blade with  $\theta_c = 8^\circ$  added.

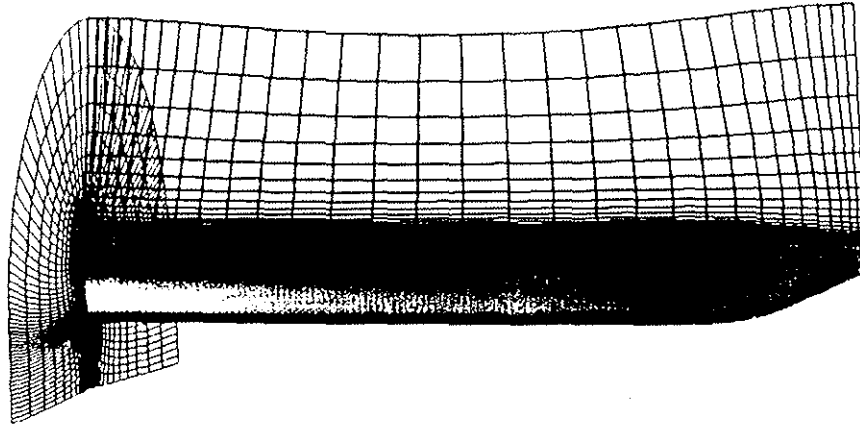


Fig. 3 A view showing the 3:1 tapered Boeing-360 rotor blade and the C-type grid wrapped around it. The grid has dimensions of 101x41x37.

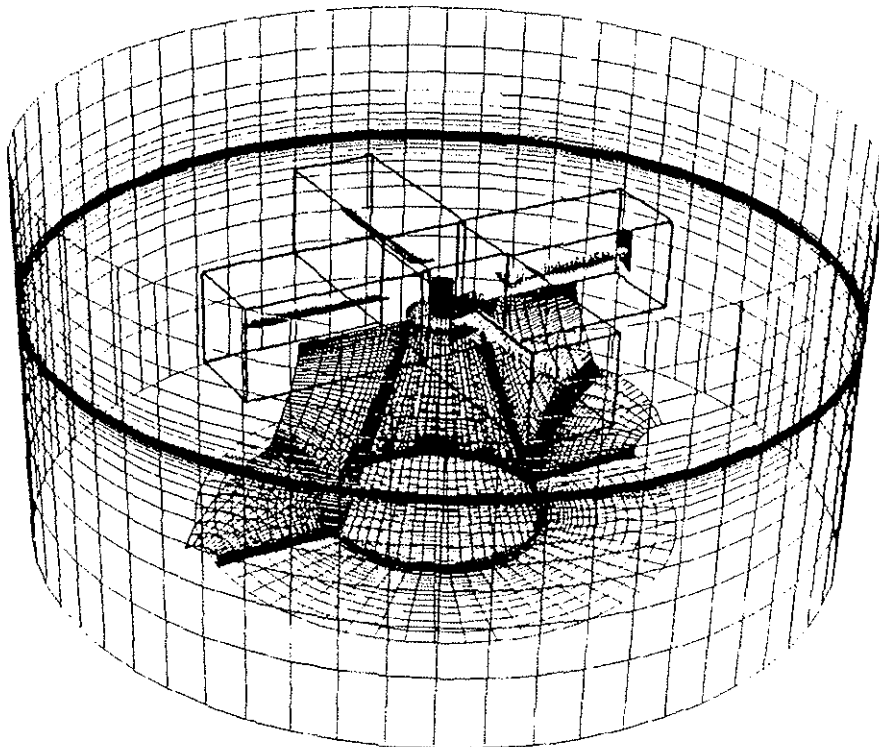
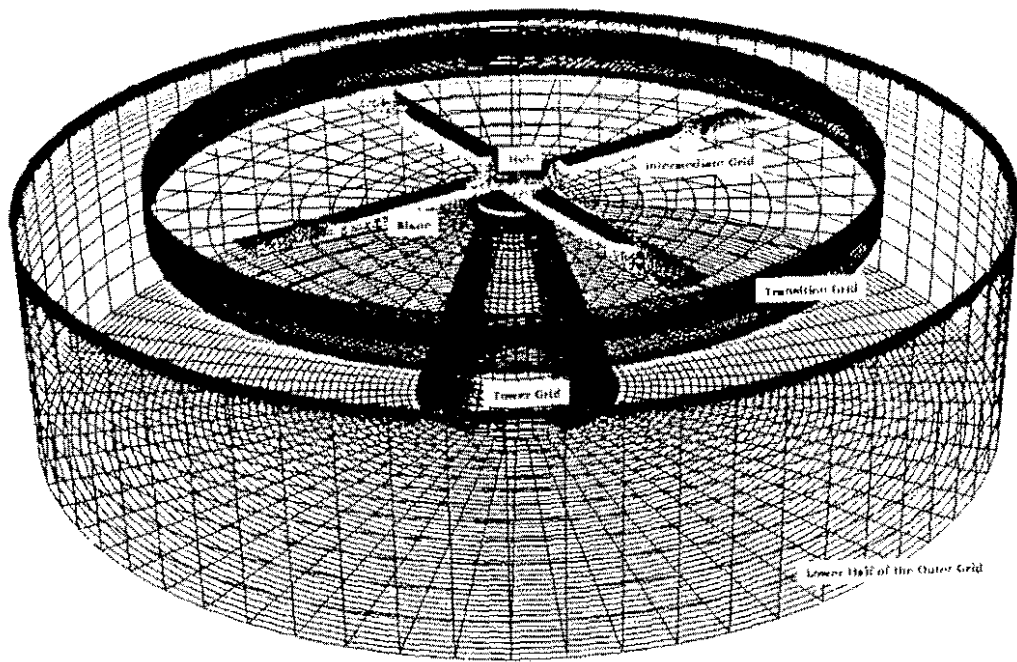


Fig. 4 Composite grid system showing the blade surface grid (light blue), blade grid (dark blue), blade transition grid boundaries, hub surface (black), tower surface (magenta), tower grid (green), and farfield global grid.



**Composite Grid System**

Fig. 5 A view of the composite grid system for the rotor-body configuration.

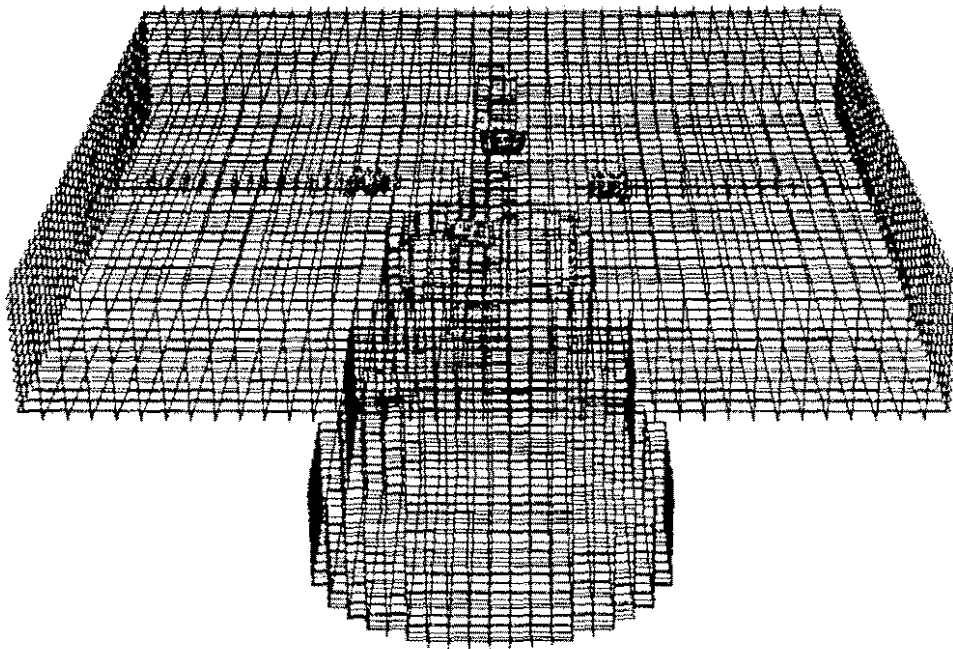


Fig. 6 A view of the Chimera hole boundaries in the composite grid system.

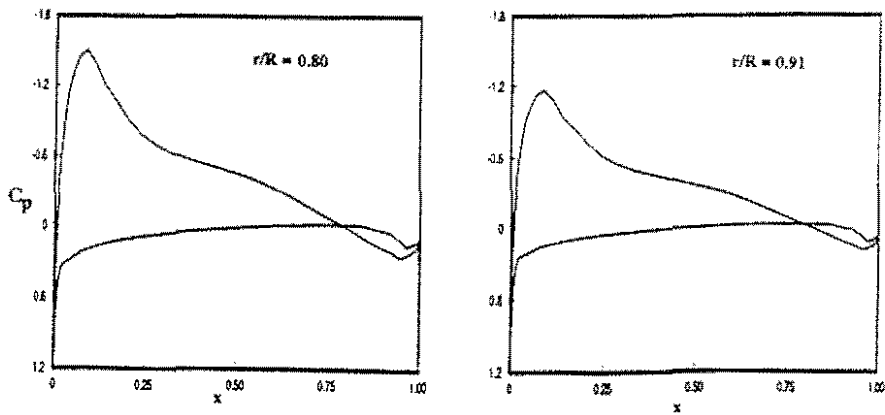


Fig. 7 Sample surface pressures on the rotor blade at two radial stations for the flow condition of  $M_{tip} = 0.63$ ,  $\theta_c = 8^\circ$ , and  $Re = 2.5 \times 10^6$ .

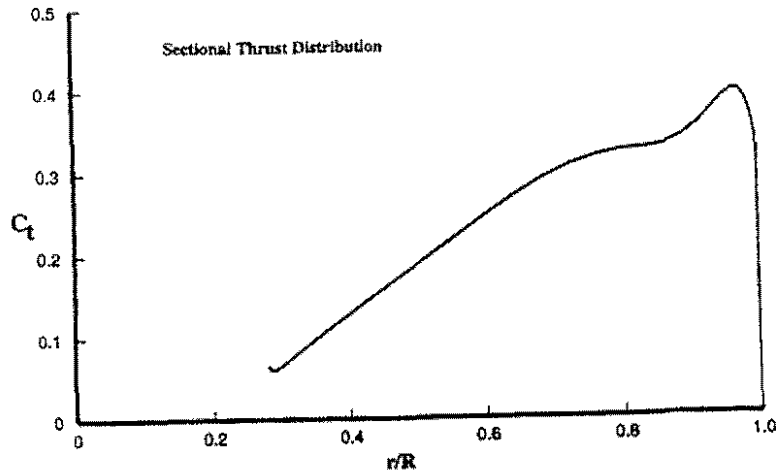


Fig. 8 Calculated sectional thrust ( $C_t$ ) distribution along the blade.

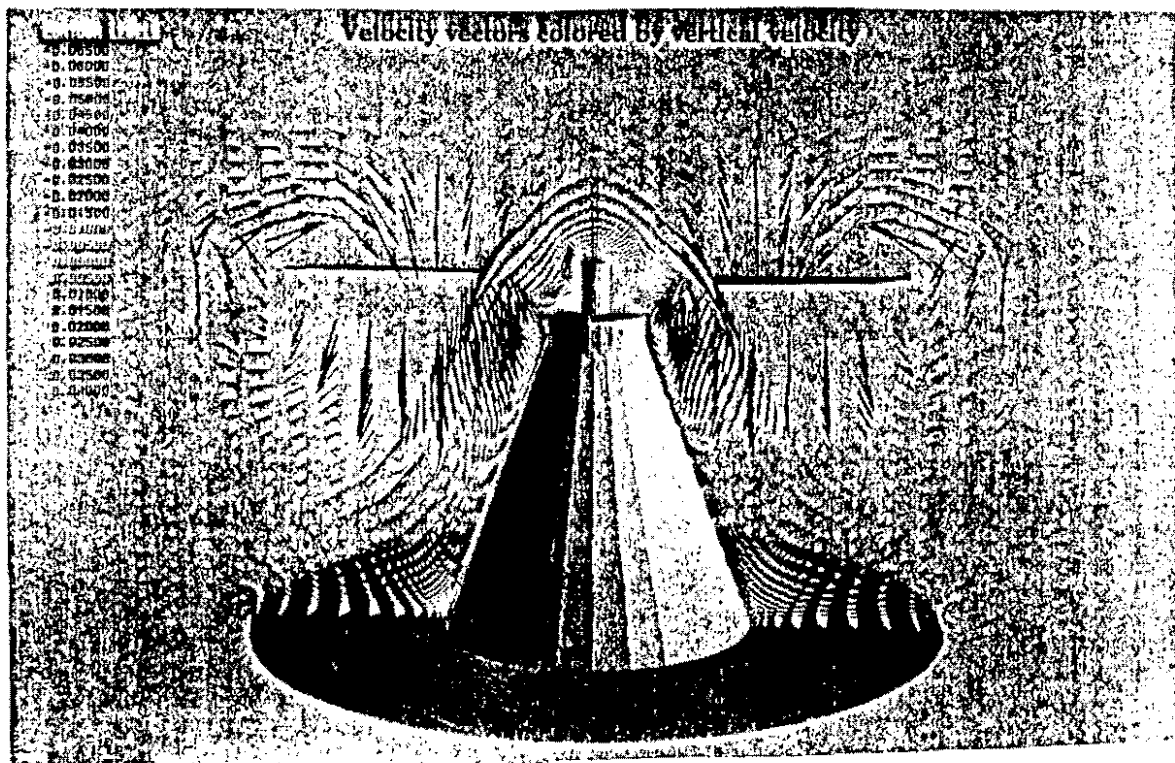


Fig.9 Plot of the velocity vectors colored by the vertical velocity on a plane cutting through the rotor axis.